Snowdrift and Accumulation on Landfast Ice Around Antarctic Icebergs: Insights from Modeling and Observational Data

Journal:	*Journal of Glaciology*
Manuscript ID	JOG-2025-0107
Manuscript Type:	Article
Date Submitted by the Author:	24-Jul-2025
Complete List of Authors:	Hames, Océane; Swiss Federal Institute for Forest Snow and Landscape Research WSL Institute for Snow and Avalanche Research; EPFL-ENAC Bouzdine, Iolène; EPFL-ENAC Helm, Veit; Alfred Wegener Institute Helmholtz Centre for Polar and Marine Research, Glaciology Haas, Christian; Alfred Wegener Institute for Marine and Polar Research, ; University of Bremen, Lehning, Michael; Swiss Federal Institute for Forest Snow and Landscape Research WSL Institute for Snow and Avalanche Research; EPFL-ENAC
Keywords:	Icebergs, Snow/ice surface processes, Sea ice, Wind-blown snow
Abstract:	Snow cover influences sea ice thermodynamics and mass balance, making its distribution and properties critical to polar research. Grounded icebergs in coastal Antarctica substantially affect surface snow distribution and landfast sea ice patterns, which has received limited scientific attention. To address this gap, this study integrates observational data with numerical snow transport simulations to investigate snow distribution on landfast ice around icebergs, emphasizing the influence of wind and iceberg size. Observations show that persistent wind directions shape characteristic snow patterns around icebergs, with substantial windward and lateral drifts and an elongated snow-depleted region in the lee. They also indicate that snowdrift size scales non-linearly with iceberg size, demonstrating reduced snow

	accumulation efficiency for larger icebergs. This trend is partially captured by the model, which also highlights the key role of wind direction shifts in reproducing observed distributions. The model further suggests that the maximum extent of snowdrifts is constrained by peak wind speeds encountered on site. Together, our findings reveal emerging links between ice shelf and fast ice processes, the use of iceberg-associated snowdrifts as proxies for local weather, and insights into the snow mass balance on Antarctic landfast ice.

Journal of Glaciology, Vol. , No. , 2025

Snowdrift and Accumulation on Landfast Ice Around Antarctic Icebergs: Insights from Modeling and Observational Data

Océane Hames[1,2], Iolène Bouzdine[2], Veit Helm[3], Christian Haas[3,4], Michael Lehning[1,2]

[1] *WSL Institute for Snow and Avalanche Research SLF, Davos, Switzerland*

[2] *School of Architecture, Civil and Environmental Engineering, Ecole Polytechnique Fédérale de Lausanne (EPFL), Alpole, Sion, Switzerland*

[3] *Alfred-Wegener-Institut (AWI), Helmholtz-Zentrum für Polar- und Meeresforschung, Bremerhaven, Germany*

[4] *Institute for Environmental Physics (IUP), University of Bremen, Bremen, Germany*

Correspondence: Océane Hames <hames.oceane@gmail.com>

ABSTRACT. Snow cover influences sea ice thermodynamics and mass balance, making its distribution and properties critical to polar research. Grounded icebergs in coastal Antarctica substantially affect surface snow distribution and landfast sea ice patterns, which has received limited scientific attention. To address this gap, this study integrates observational data with numerical snow transport simulations to investigate snow distribution on landfast ice around icebergs, emphasizing the influence of wind and iceberg size. Observations show that persistent wind directions shape characteristic snow patterns around icebergs, with substantial windward and lateral drifts and an elongated snow-depleted region in the lee. They also indicate that snowdrift size scales non-linearly with iceberg size, demonstrating reduced snow accumulation efficiency for larger icebergs. This trend is partially captured by the model, which also highlights the key role of wind direction shifts in reproducing observed distributions. The model further suggests that the maximum extent of snowdrifts is constrained by peak wind speeds encountered on site. Together, our findings reveal emerging links between ice shelf and fast ice processes, the

use of iceberg-associated snowdrifts as proxies for local weather, and insights into the snow mass balance on Antarctic landfast ice.

1 INTRODUCTION

In Antarctic coastal regions, landfast sea ice (also known as fast ice) forms a stationary extension of the cryosphere, attached to the shoreline, ice shelves, or grounded icebergs. It plays a central role in stabilizing ice shelves by providing buttressing, damping wave energy, and promoting surface cooling, all of which reduce stress and deformation within the ice sheet system (Massom and others, 2010). Biologically, persistent fast ice supports marine ecosystems by influencing species distribution, trophic dynamics, and nutrient exchange (Nihashi and Ohshima, 2015). For marine operations, its stability and seasonal predictability are critical for navigation, over-ice access, and logistical planning (Fraser and others, 2021). Landfast ice also regulates energy fluxes at the ocean-atmosphere interface, affecting local atmospheric conditions and contributing to larger-scale climate feedbacks (Achter and others, 2022). Together, these functions demonstrate the critical role of landfast ice in sustaining the structural and ecological integrity of Antarctic coastal regions.

The snow mass balance in coastal Antarctica is shaped by unique conditions of snow accumulation and redistribution. Studies show that blowing snow often reshapes the snow cover on landfast ice, where snow depths are typically shallow (Fraser and others, 2023; Lei and others, 2010). Specifically, icebergs influence snow distribution over Antarctic fast ice through various physical processes, with the resulting snow cover having broader ecological and climatic consequences. Research indicates that wind dynamics around icebergs generate localized turbulence, resulting in larger snowdrifts and uneven snow distribution on the ice (Franke and others, 2025; Fraser and others, 2023). In addition, the size and mass of icebergs create shading effects, impacting solar radiation absorption and consequently affecting snowpack melting and refreezing (Nihashi and Ohshima, 2015). These processes collectively drive the metamorphism of snow grains, which strongly affects the snow cover's insulating capacity and, in turn, the thermal behavior and melt patterns of the ice during warmer months (Zhao and others, 2022). Overall, icebergs may play a key role in shaping the physical and structural characteristics of snow cover on Antarctic landfast ice —by altering wind and light exposure— yet the exact impact of this modified snow cover on sensitive polar environments remains understudied.

Franke and others (2025) combined ultra-wideband microwave (UWBM) snow radar and laser scanner observations to investigate icebergs embedded in fast ice. Their findings reveal persistent snow distribution patterns, including thick snowdrifts on the windward side of icebergs, elongated lateral drifts aligned with prevailing winds, and virtually snow-free zones with exposed rough ice in the lee. Increased cross-polarized backscatter in the UWBM data further indicates that snow loading induces basal flooding and slush formation beneath these drifts. Building on this work, the present study examines how icebergs influence wind dynamics and the subsequent effects on snow distribution. A key knowledge gap concerns the role of iceberg size and shape in controlling snowdrift formation, as well as the impact of wind conditions on accumulation patterns and volumes. Previous studies on snow accumulation around obstacles suggest that turbulence and obstacle geometry are critical factors, but their relevance in iceberg-dominated environments remains poorly understood.

In this context, snow modeling frameworks become especially useful. Extensive experimental and theoretical research has been carried out to develop parameterizations for snow transport over flat terrain (e.g. Comola and Lehning, 2017; Doorschot and Lehning, 2002; Pomeroy and Gray, 1990), which were later integrated into numerical models (e.g. Sharma and others, 2018; Groot Zwaaftink and others, 2013). These foundational studies paved the way for developing numerical models that integrate structures into wind–snow simulations (Tominaga, 2018). Two widely used methods are the Eulerian–Eulerian (E–E) and Eulerian–Lagrangian (E–L) approaches. While E–E frameworks are computationally efficient and have shown reliable performance (e.g. Tominaga and others, 2011; Beyers, 2004), the E–L method offers superior resolution of particle–fluid momentum exchange and complex near-surface dynamics (Wang and Huang, 2017). This approach has been used in earlier studies of snowdrift processes, enabling the separate assessment of individual driving factors (Hames and others, 2025). In light of its advantages, the E–L method is used in this study.

This research addresses the influence of iceberg size and wind conditions on snow distribution around Antarctic icebergs embedded in fast ice, using the Eulerian–Lagrangian snow transport model *snowBedFoam*. Following its earlier use in Arctic sea ice (Hames and others, 2022) and polar research station simulations (Hames and others, 2025), the model is used here for the first time to simulate snowdrift formation around Antarctic icebergs, leveraging its ability to resolve near-surface, microscale snow particle dynamics around complex bodies. Correctly representing larger-scale icebergs is a methodological challenge in E-L set-ups, which is successfully addressed in this study. A digital elevation model (DEM) from an airborne field campaign in East Antarctica (Franke and others, 2025) provides the simulation topography and serves for comparison with model outputs. Using this setup, we simulate a range of iceberg sizes and wind forcing scenarios to assess their qualitative and quantitative effects on snow accumulation. This work is organized as follows: first, the data and the approach used to identify icebergs and snowdrifts are described, followed by an introduction of the snow transport model. Then, results focusing on wind forcing and iceberg size are discussed, along with broader implications and conclusions. Overall, our findings shed light on how icebergs influence snow distribution on landfast ice and provide notable insight into the broader interactions between sea ice, ice shelves, and snow mass balance in Antarctic coastal regions.

2 DATA

Extensive observations of landfast sea ice and snow thickness, along with platelet ice occurrence and depth, were conducted along the coast of Dronning Maud Land during the “Antarctic Sea Ice: Thickness, Melt Ponding, and Ice Shelf Interaction” (ANTSI) airborne campaign in November−December 2022 (Franke and others, 2025; Haas, 2023). Part of the surveys were carried out over the landfast ice of Atka Bay (Figure 1.A), a prominent embayment about 25 km wide and up to 20 km long in the Ekström Ice Shelf at approximately 8° west, near the German research station Neumayer III (Wesche and others, 2016). This bay typically hosts icebergs of various sizes and shapes. Here, we use digital elevation models derived from airborne laser scanner (ALS) measurements to retrieve iceberg sizes and shapes (Figure 1B), while the analysis of complementary sensors —including snow radar as well as visible (VIS) and near-infrared (NIR) cameras— was previously detailed by Franke and others (2025). The ALS system used was a RIEGL LMS-VQ580 laser scanner operating at a near-infrared wavelength of 1064 nm, with a scan angle of 60°. To achieve high spatial resolution in the surface reflection point clouds, surveys were conducted at an altitude of approximately 360 m. Given that the swath width was roughly equal to the survey altitude, complete mapping of the entire bay was not feasible. Instead, multiple parallel, closely spaced survey lines focusing exclusively on the most prominent icebergs and their associated snowdrifts were carried out (Figure 1B). Data processing included correction for aircraft altitude and attitude variations using GNSS and IMU data, projection of the DEM onto the WGS84 ellipsoid, and adjustments of small elevation differences between swaths (Franke and others, 2025; Hutter and others, 2023). Eventually, a DEM with a grid resolution of 1×1 m and an accuracy of ellipsoidal heights of 0.05 m was generated and served as a numerical base for the snow transport simulations.

The final DEM includes 33 icebergs, of which 25 were analyzed in more detail (see Methods, Section 3.1). Four of these were subsequently selected for the modeling analysis, numbered 1 through 4 in Figure 1.C. Their locations in Atka Bay are depicted in subpanel B, with corresponding white numbers and ellipses highlighting their positions. These icebergs were chosen for their diverse shapes, ranging from round (Iceberg 4) to elliptical (Icebergs 1 and 3) to triangular (Iceberg 2), with both flat and curved windward and lateral faces. Note that differentiating between ice and snow in the digital elevation model can be difficult, as drifting snow can settle close to the icebergs, forming a continuous surface between the sea ice and their sides.

Atka Bay constitutes an ideal location for drifting snow studies, as it experiences very steady wind conditions with dominant easterly winds (80–100°) occurring on approximately 45% of days (Klöwer and others, 2013). This shapes the snowdrifts into stable features, making them suitable for study and replication in numerical models. This ideal scenario reduces the number of simulations required to accurately replicate the drift patterns and allows to study the cumulative consequences of wind redistribution which would otherwise be blurred. Moreover, the presence of icebergs within the ice introduces significant variability in snow depth and properties, providing valuable insights into their effect on the sea ice beneath.

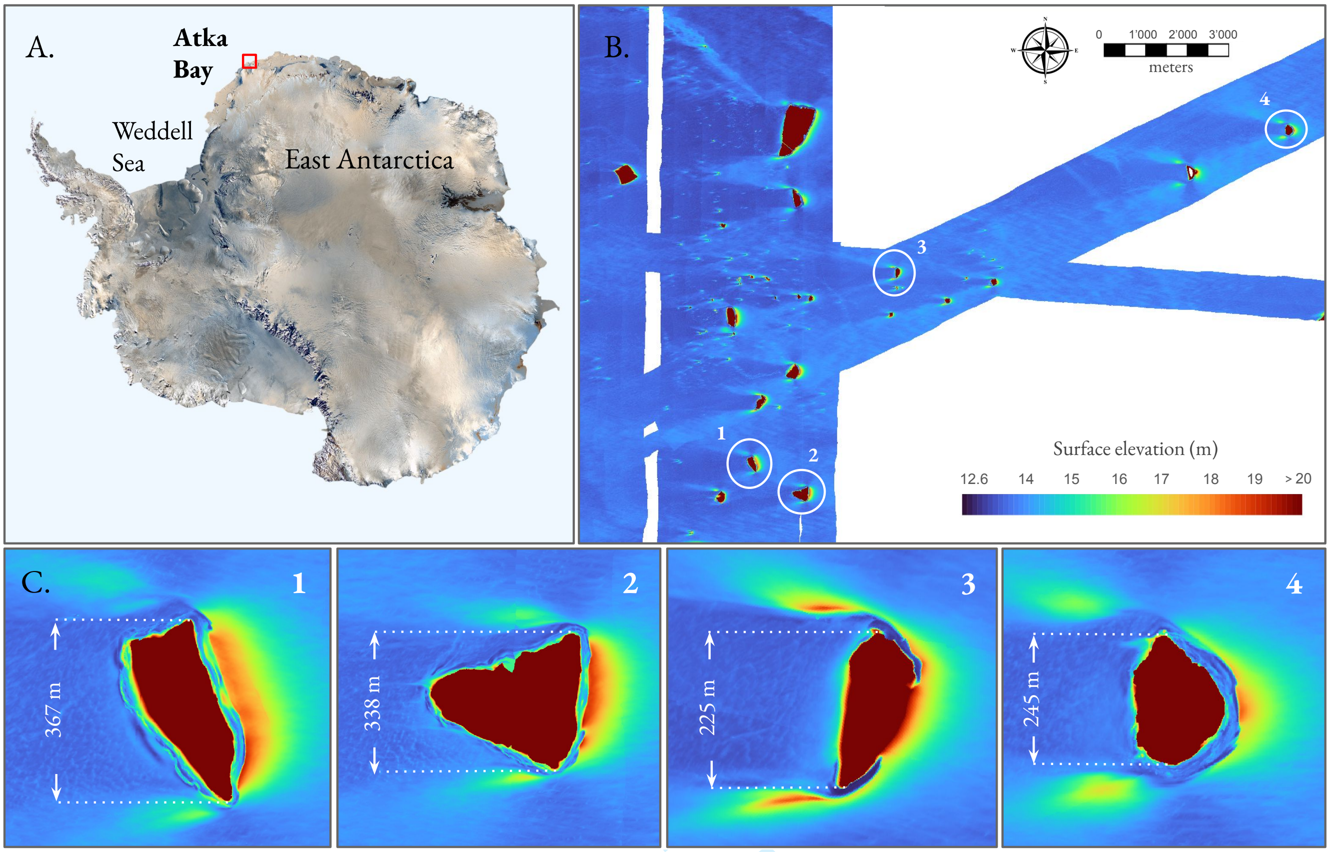

Fig. 1. **A.** Map of Antarctica with the study site of Atka Bay highlighted by the top red square. **B.** Digital elevation model of Atka Bay featuring landfast sea ice and icebergs. Elevations are given as WGS84 ellipsoidal heights. The white numbers (1-4) and ellipses display the locations of the icebergs shown in the bottom panel. Snowdrifts indicate the dominant wind direction, blowing from right (east) to left (west). **C.** Detailed views of the four icebergs selected for the model runs. The maximum horizontal extent is marked by the dotted arrows. Note that the dimensional scale is not respected here.

3 METHODS

3.1 Snowdrift and iceberg retrievals

Icebergs were detected in the digital elevation model using a combination of gradient- and elevation-based thresholding. For both parameters, the threshold was defined as $\mu + k \cdot \sigma$, where μ and σ represent the mean and standard deviation of either gradient or elevation, and k is set to 1. First, areas with sharp elevation changes — typically marking iceberg edges — were identified using gradient magnitude analysis. These initial detections were further refined by applying an elevation threshold, preserving only regions satisfying both criteria. This approach enables the inclusion of areas with substantial elevation change while excluding low-relief regions likely associated with snowdrifts or minor terrain features. Further morphological operations were applied to refine iceberg contours, supplemented by geometric filters based on compactness and aspect ratio, resulting in an initial selection of 33 icebergs. Subsequently, some icebergs were excluded based on the following criteria: (1) close proximity to other icebergs, (2) highly irregular or fragmented shapes, and (3) insufficient size, making distinction between the icebergs and their associated snowdrifts difficult. This final exclusion process resulted in the selection of 25 icebergs for subsequent analysis.

Following detection, each iceberg was spatially associated with a proximal region of snow accumulation. Assuming that the snow in Atka Bay is generally level in the absence of pressure ridges or icebergs with average thicknesses of 0.8 m (Arndt and others, 2020), statistically significant deposition zones around icebergs were identified and analyzed to evaluate their structural and quantitative characteristics. As a first step, regions prone to snow accumulation were outlined using elliptical zones centered on each iceberg and aligned with the prevailing wind direction. The dimensions of these ellipses were set proportional to the square root of the iceberg's area, such as $a = 3 \cdot \sqrt{Area}$ and $b = 2 \cdot \sqrt{Area}$ where a and b represent the semi-major and semi-minor axes of the ellipse, respectively. Then, height anomalies within each of these ellipses were detected using a z-score threshold, where z is defined as $z = (x - \mu)/\sigma$ with x the observed value, μ the mean elevation and σ the standard deviation of the surface elevation field. A threshold of $z > 1$ was used to isolate areas of pronounced snow accumulation in the observations. Similarly, this approach was applied to analyze snowdrifts in the numerical results, relying on preliminary ellipses and snow distribution values with $z > 1$ to inform the analysis.

The snowdrifts retrieved with the method above provide a basis for comparing model output with observational data. For easier comparison, the snowdrift structure is sorted into distinct regions based on their position relative to the wind (windward, leeward or lateral). The goal is to understand the influence of iceberg size and wind conditions on snowdrift patterns and quantities by combining both observations and numerical simulations. To properly interpret the results, it is necessary to test whether the model successfully replicates the spatial distribution of snowdrifts and the iceberg–snowdrift scaling relationship observed in the data, thereby highlighting potential limitations. Further details can be found in Section 3.4, along with the model runs.

3.2 Snow transport model

The numerical experiments in this study were performed using the snow transport model snowBedFoam (Hames and others, 2021). This model has been previously applied to Arctic sea ice (Hames and others, 2022) and to an Antarctic research station (Hames and others, 2025). Here, it is extended to iceberg-scale structures for the first time, introducing new computational challenges due to the increased model scale. The Atka Bay iceberg dataset offers a unique opportunity to quantitatively evaluate model performance by comparing the observed and simulated scaling relationships between iceberg and snowdrift areas (see Sections 3.4 and 4.2). Additionally, the presence of multiple icebergs exposed to similar wind conditions provides a robust sample to assess consistent model behavior across different obstacles. This enhances the dataset with numerous snowdrift observations under comparable wind regimes, helping to identify recurring model limitations. Notably, the comparison highlighted the importance of incorporating wind direction variability to simulate lateral flow effects, suggesting a promising pathway for improving snowdrift reproducibility in future work (Section 4.1).

snowBedFoam is a fluid dynamics-based drifting snow model extended from the DPMFoam solver in OpenFOAM (The OpenFOAM Foundation, 2021). The DPMFoam solver is specifically designed to simulate discrete phase models (DPM), which describe the interactions between a continuous fluid phase (e.g., air) and dispersed discrete particles (e.g., snow) (Fernandes and others, 2018). Given its prior presentation, we only provide a brief overview of the snow model used in the simulations. The governing equations for the snow and fluid systems are comprehensively detailed in earlier publications (Hames and others, 2022; Melo and others, 2022; Sharma and others, 2018). In snowBedFoam, the implemented equations parametrize the three main modes of snow saltation, which involve the lifting of snow particles by wind shear (*aerodynamic entrainment*), the bouncing of particles upon impact with the surface (*rebound*) and the ejection of snow particles caused by collision with other grains (*splash*). The amount of particles eroded by aerodynamic entrainment is computed using Bagnold's shear stress threshold (Bagnold, 1941) and a parametrization developed by Anderson and Haff (1991). Rebound entrainment is modeled using a rebound probability approach developed by Anderson and Haff (1991) and adapted to snow based on the work of various authors (Groot Zwaaftink and others, 2013; Doorschot and Lehning, 2002). The equations for splash entrainment were developed by Comola and Lehning (2017); they are conditioned by bed cohesion, particle diameter and velocity, particle ejection angles and impact energy (momentum) fractions. Together, these parameterizations govern the exchange of snow particles between the snowbed and the overlying air. Along with solving the Navier–Stokes equations around icebergs, particle–fluid interactions are computed, resulting in snow distribution patterns shaped by the integrated influence of airflow, iceberg geometry, and snow transport dynamics.

The finite volume method (FVM) is employed for numerical discretization in our snow simulations (Moukalled and others, 2015). We use a statistically steady representation of a neutrally-stratified turbulent flow by solving the Reynolds-Averaged Navier-Stokes (RANS) equations (Pope, 2000). The Reynolds stress tensor is calculated using the standard two-equation closure model k-ϵ (Launder and Spalding, 1974), which solves two supplementary transport equations for turbulent kinetic energy (k) and turbulent dissipation rate (ϵ). The spatial discretization of the gradient and divergence terms in the conservation equations is performed using the Gauss linear and bounded Gauss linear upwind schemes, respectively. Time integration of the transient terms is achieved using the Euler method (Moukalled and others, 2015). The flow time step is automatically controlled using the “*adjustableRunTime*" approach available in OpenFOAM, which adapts the time step based on the maximum Courant number. More information regarding the adjustable time step method for the flow is available in the OpenFOAM documentation and source code (The OpenFOAM Foundation, 2025b).

The movement of snow particles within the domain is modeled using the Lagrangian particle tracking method, which integrates the flow behavior. To optimize computational efficiency, particles are grouped into parcels of similar size and trajectory. Particles within a single parcel are either entrained simultaneously at the same location and time or ejected together during the same splash event. The Eulerian quantities at each parcel's location are linearly interpolated using the closest cell point values based on inverse distance weighting. Parcel motion is captured through the “face-to-face tracking algorithm", which adjusts the Lagrangian time step as particles cross cell boundaries. For simplicity, we account for gravity and fluid-particle drag forces to compute the grain trajectories. Initially, the particles are introduced into the domain via aerodynamic entrainment. Once the snow parcels are aloft, the rebound-splash module is activated whenever a parcel impacts the surface, resolving the micro-scale ejection of grains from the snowbed.

3.3 Numerical settings

Figure 2.A shows an example of the numerical domain used in the simulations, with Iceberg 3 as a reference. The extents of the domain in the longitudinal (x), lateral (y) and vertical (z) directions were defined based on the guidelines proposed by Franke and Baklanov (2007), which relate domain dimensions to the

maximum height (H) of the simulated object. The maximum heights of the four icebergs are 35 m (iceberg 1), 28 m (iceberg 2), 24 m (iceberg 3), and 39 m (iceberg 4). The extent of the modeled icebergs in all directions is reported in Table A2 (Appendix). In the longitudinal direction, the domain extends 8H upstream for the approach flow and 20H downstream to capture the wake region behind the iceberg. In both the lateral and vertical directions, a distance of 5H separates the iceberg from the domain walls. The chosen extents are considered sufficiently large to minimize the influence of domain boundaries on the flow around the iceberg. Simulations were conducted using an unstructured grid with a predominance of hexahedron cells. Various mesh sizes were tested, and the final configuration was selected based on computational efficiency and result consistency with finer grids. Each test result was also compared to observational data to ensure the simulated patterns aligned with the observations. The final mesh resolution reaches 2 m in the far-field and refines to 0.5 m near the ground and iceberg walls. As a result, the total cell count ranges from 14.5 to 43 million, depending on the shape and dimensions of the iceberg. The different iceberg sizes in Figure 2.B were modeled by uniformly scaling the reference meshes to the desired dimensions, resulting in lateral iceberg extents ranging from 125 to 1500 m.

Detailed values for model coefficients as well as wind and snow particle properties are provided in Table A1 (Appendix). The boundary conditions (BCs) set in the simulations are shown in Figure 2.A for the fluid and particle phases. Flow-related conditions are depicted in the colored boxes, each representing a specific patch. At the inlet (pink), height-dependent profiles of velocity and turbulence parameters (k, ϵ) are applied, based on a generalized neutral atmospheric boundary layer (ABL) profile. The profile calculations, linked to the $k-\epsilon$ model and introduced by Richards and Hoxey (1993), take the wind speed vector at 10 m as input parameter. Nominal values are applied for wind speed, while the wind direction is inferred from the drift observations. At the outlet patch (purple), a pressure outlet condition is applied to define the pressure at the boundary, while a zero-gradient condition is used for the other variables. At the side patches (light green), zero-gradient conditions are applied to all variables, which is appropriate for open domain sides where flow influence is negligible. No-slip BCs are used for the velocity at the snowbed (teal) and iceberg patches, while zero-gradient is used at the top boundary. The turbulent quantities and turbulent viscosity (ν_f) at the ground are constrained with wall functions specific to the ABL and consistent with the inlet condition according to the work of Hargreaves and Wright (2007). The ν_t values are calculated using standard rough wall functions, using the aerodynamic surface roughness z_0 as roughness wall parameter. Further details can be found in the OpenFOAM documentation and in the source code (The OpenFOAM

Foundation, 2025a). Besides, boundary conditions related to particles are indicated by the round symbols at each patch (Figure 2.A). The aerodynamic entrainment and rebound-splash modules are enabled for the snowbed (ground) patch only. At the iceberg walls, particles are set to rebound, while they exit the domain at the lateral and top boundaries.

All simulations are initialized with fully developed Eulerian flow fields obtained after 100 seconds of flow-only simulation. These steady-state wind fields are then employed as the initial conditions for the subsequent Eulerian-Lagrangian simulations, which include a comprehensive representation of snow particle dynamics. Simulations were run until the system's total mass stabilized, signaling steady-state erosion and deposition. This occurred in all cases by 300 seconds, which was set as the final simulation time.

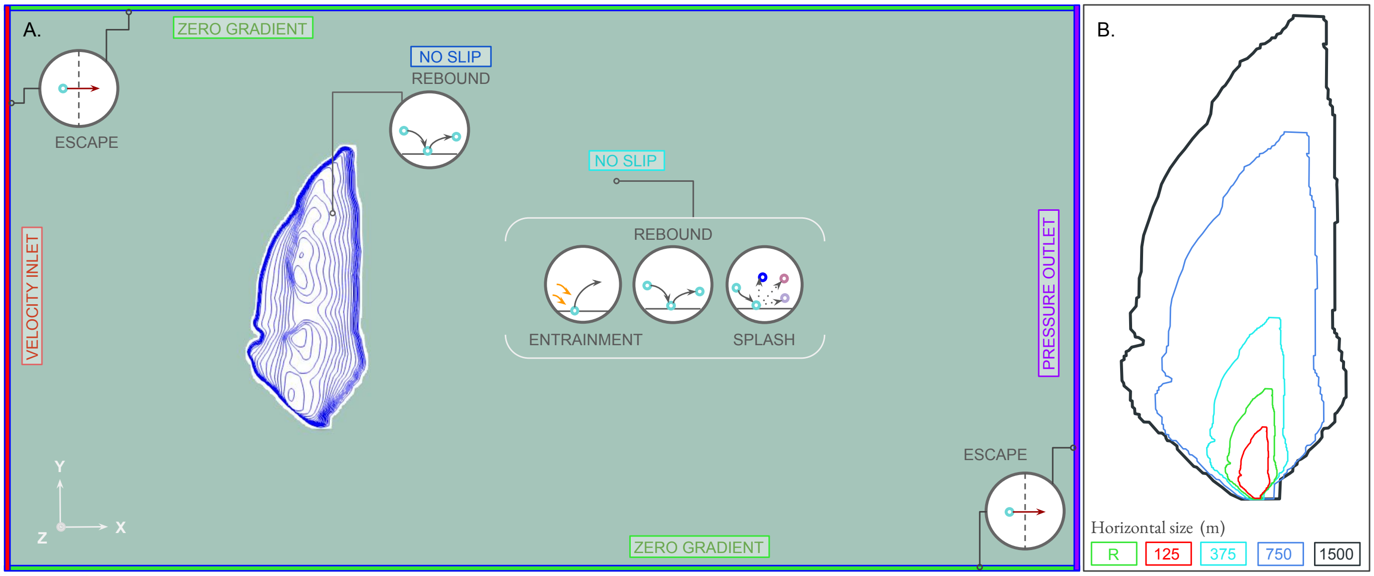

Fig. 2. **A.** Numerical domain and boundary conditions for the snowBedFoam simulations. The labels within the frames correspond to the fluid phase, while the conditions inside the circles refer to snow particles. Wind blows from left to right. **B.** Relative scale of the five iceberg sizes tested in the simulations. The size is defined by the length of the maximum horizontal dimension, as shown in the colored rectangles at the bottom of the figure.

3.4 Model runs

Rather than modeling snowdrift formation across the entire Atka Bay, we selected four representative icebergs to reduce computational demand and complexity. These icebergs were chosen to capture the diversity in shape and snowdrift patterns observed in the region, providing a representative basis for analysis. Each iceberg served as the starting point for simulations with varying wind conditions to assess their impact on snowdrift structure. Additionally, the iceberg dimensions were numerically modified to investigate the effect of iceberg size on the snow distribution and to separate the size effect from shape. Table 1 presents a typical set of simulations associated with Iceberg 1, while a comprehensive overview covering all selected icebergs is provided in Table A2 (Appendix). The generic run name begins with the iceberg identifier as defined in Figure 1 (“icb”), followed by its size classification (“size”), the wind speed (“ws”) and wind direction (“wd”). The first bold row corresponds to the simulation with the original iceberg dimensions (size 1), a standard wind speed of 10 m.s^{-1}, and a normal wind direction inferred from the drift patterns. The subsequent rows correspond to variations in wind speed, wind direction, and iceberg size. Size classes are defined based on lateral dimension (Y) as follows: 1 – reference size, 2 – 125 m, 3 –

375 m, 4 – 750 m, and 5 – 1500 m. These values stem from the iceberg size categories described by Orheim and others (2022), as part of the SCAR (Scientific Committee on Antarctic Research) International Iceberg Database. For each size class, iceberg dimensions were uniformly scaled using the ratio of the target to the original lateral dimension. Note that the wind direction results (run wd5) are derived from combining two runs, each with opposing 5° deviations from the longitudinal axis. Simulations at a lower wind speed (5 $m.s^{-1}$) were conducted in parallel to the 10 and 15 $m.s^{-1}$ runs (ws10, ws15), but were excluded from the main analysis due to the very limited snow redistribution observed.

Each model run is subsequently compared to the observations. Reference simulations using the original iceberg size and varying wind forcing are compared to surface elevation data, providing a range of weather conditions against which observations can be evaluated (Section 4.1). Then, numerical experiments involving icebergs of various sizes are compiled and compared with the full snowdrift and iceberg datasets, highlighting the scaling relationship between iceberg and snowdrift sizes (Section 4.2).

Table 1. Model runs performed for Iceberg 1, with the reference simulation highlighted in bold. A detailed table containing the simulation settings for all icebergs is provided in the Appendix (Table A2).

Run name	Iceberg	Size class	Dimensions (m)			Wind speed (m.s^{-1})	Wind direction (°)
			X	Y	H		
icb1_size1_ws10_wd0	**1**	**ref**	**214**	**367**	**35**	**10**	**0**
icb1_size1_ws15_wd0	1	ref	·	·	·	15	0
icb1_size1_ws10_wd5	1	ref	·	·	·	10	avg(5, −5)
icb1_size2_ws10_wd0	1	2	73	125	12	10	0
icb1_size3_ws10_wd0	1	3	219	375	36	10	0
icb1_size4_ws10_wd0	1	4	437	750	72	10	0
icb1_size5_ws10_wd0	1	5	877	1500	144	10	0

4 RESULTS

4.1 Snowdrifts: Observations vs. Model

Model simulations at the original iceberg scale were carried out to compare with measurements and assess whether the wind-driven snow transport model can reproduce the snow distribution patterns observed around icebergs. This helps evaluate model performance and supports further analysis of relevant snowdrift processes. Figure 3 shows the four icebergs selected for the simulations, with observational data presented in the first column and corresponding model outputs displayed in the three subsequent columns. The model results include, from left to right: simulations using the reference conditions (icb_size1_ws10_wd0), simulations with two wind direction adjustments of +5° and −5° (icb_size1_ws10_wd5), and simulations with increased wind speed (icb_size1_ws15_wd0). Adjusting wind direction is intended to compensate for the limited ability of the RANS model to resolve lateral variations in wind direction, such as those caused by turbulence. The simulation outputs are oriented to match the observations, with the wind blowing from the right. The snow mass distribution is expressed in kg.m^{-2}, with blue representing snow erosion and red showing deposition. To facilitate comparison, the snowdrift pattern is categorized into distinct regions according to their position relative to the wind. The black letters in Figure 3 (**A**-**D**) indicate these specific zones and are highlighted in bold throughout the text. In addition, white symbols (circle, triangle, square) are included in the plots to highlight specific, small-scale features. Overall, snowdrift patterns around icebergs exhibit consistent characteristics: a wide, uniform snowdrift on the windward side (**A**); two lateral snowdrifts forming along the sides and extending downwind (**B**, **C**); and a small, localized accumulation zone positioned directly in the lee of icebergs (**D**). Examining the windward accumulation on the righthand side, all icebergs exhibit a narrow wind scoop (i.e., a snow-free area at their base), which is accurately reproduced in the simulations. As wind speed increases, the extent of this windward wind scoop decreases, causing the snow accumulation to move closer to the icebergs. For iceberg 3, at higher wind speeds, the snow accumulation directly contacts the iceberg in certain locations, which may explain the formation of the "snow bridge" observed in the data (triangle symbol). Iceberg 4 also exhibits a distinct feature in the upper portion of zone **A** (circle symbol), where a pronounced accumulation band extends across the erosion zone in simulations with higher wind speeds. This feature is also reflected in the measurements, as the green elevation contour intersects the snow-free (blue) region at the corresponding location. Simulations indicate that snow accumulation on the windward side grows with wind speed, implying that the observations reflect accumulation under various wind conditions, with the strongest winds being the key factor influencing the maximum drift extent.

Focusing on the two accumulation zones at the flanks (**B**, **C**), simulations with (artificially) varying wind directions produce more accumulation streaks, covering a larger lateral area, which better matches the observations. Although only two additional wind directions were tested here, natural flows influenced by large-scale atmospheric turbulence would involve a broader range of directions, leading to the wider lateral side drifts seen in the measurements. An increase in wind speed leads to a more pronounced development of the lateral drifts, characterized by greater spatial spread in both the wind and crosswind directions, along with higher accumulation quantities. The resulting drift patterns align more closely with the measurement data. Notably, the accumulation observed along the upper edge of Iceberg 2 (side **C**, circle symbol) is well replicated by the model. Moreover, areas of erosion predicted by the model closely match the snow-free regions observed in the measurements, suggesting that the model effectively captures the flow dynamics around the iceberg edges. In particular, the erosion at the edges of Iceberg 1 (circle, triangle symbols) is well replicated. Other remarkable features include the erosion zone at the upper edge of Iceberg 3 (circle symbol) as well as the pronounced erosion streak on the inner side of lateral drift **B** (square), which are also reproduced in the model at the same locations.

Lastly, accumulation in the direct lee of the icebergs (zone **D**) is considered. The model generally overestimates deposition in this area, especially at higher wind speeds. Although observations also show snow accumulation at these locations, the quantities are lower, as indicated by the less intense green tones in the elevation data. In simulations with varying wind directions, accumulation in zone **D** generally appears more limited in extent, as erosion from one wind direction tends to counteract the deposition patterns generated by the other. These findings suggest that naturally variable wind directions in reality may be a key factor in the limited accumulation observed in the measurements. Snow deposited under one wind direction is likely to be eroded by subsequent winds from another direction. This is supported by the simulations showing that direct lee areas undergo stronger erosion (blue zone) than other regions, making snow accumulation there particularly vulnerable to removal during wind shifts. Another possible explanation for this overestimation involves atmospheric stability in real conditions, which likely differs from the neutral profile assumed in the simulations. Under stable conditions, reduced buoyancy and suppressed turbulence in the lee of the icebergs would likely lead to decreased snow deposition compared to the more turbulent flow in neutral simulations. Despite a reduced extent in the measurements, distinct accumulation features still emerge in lee zone **D**. For Iceberg 2, accumulation streaks appear just behind the leeward tip (triangle, square symbols), a pattern that is also reflected in the simulations, although with a greater spread. Similarly, for Iceberg 4, green accumulation bands at the base of the lee side show good alignment between model and observations (square, triangle). Among all icebergs, Iceberg 3 exhibits the highest accumulation in zone **D**, potentially due to airflow being channeled between the two highest crest points (see Figure 4), forming a pass that accelerates the flow.

To gain a deeper understanding of flow behaviour around icebergs and its influence on snow distribution, Figure 4 presents surface friction velocity fields (subpanels A and B) and flow streamlines (subpanels C and D) around Iceberg 3 for wind direction adjustments of $+5°$ and $-5°$. This comparison seeks to highlight how minor variations in wind direction influence the flow behaviour around icebergs and, in turn, affect the distribution of surface friction velocity and snow. Bold numbers in the figure and the accompanying text highlight specific regions of interest in the flow field. The upper panels reveal that zones of high (**5**) and low (**1**) surface friction velocity in the lee shift spatially depending on wind direction. These shifts reflect changes in the flow structure in the iceberg's wake, as illustrated by the streamlines in the lower panels, which directly influence the resulting snow distribution patterns. This effect is also evident along the iceberg's sides (**4**), where the high-velocity streaks deform and reorient depending on wind direction. Under conditions of a stable, stratified atmospheric boundary layer—common in Antarctica—turbulent motions are suppressed (González and others, 2024). This reduction in turbulence would lead to fewer coherent structures in the wake and may cause the flow to reattach more quickly in the lee of the iceberg, potentially increasing local surface shear stress. In addition, the suppression of vertical mixing would concentrate particles near the surface (Tomas and others, 2016), enhancing snow deposition on the windward side (**2**) and reducing the deposition potential in the lee. Such mechanisms may explain why minimal snow accumulation occurs in the lee of icebergs, a pattern that neutral stratification models fail to capture.

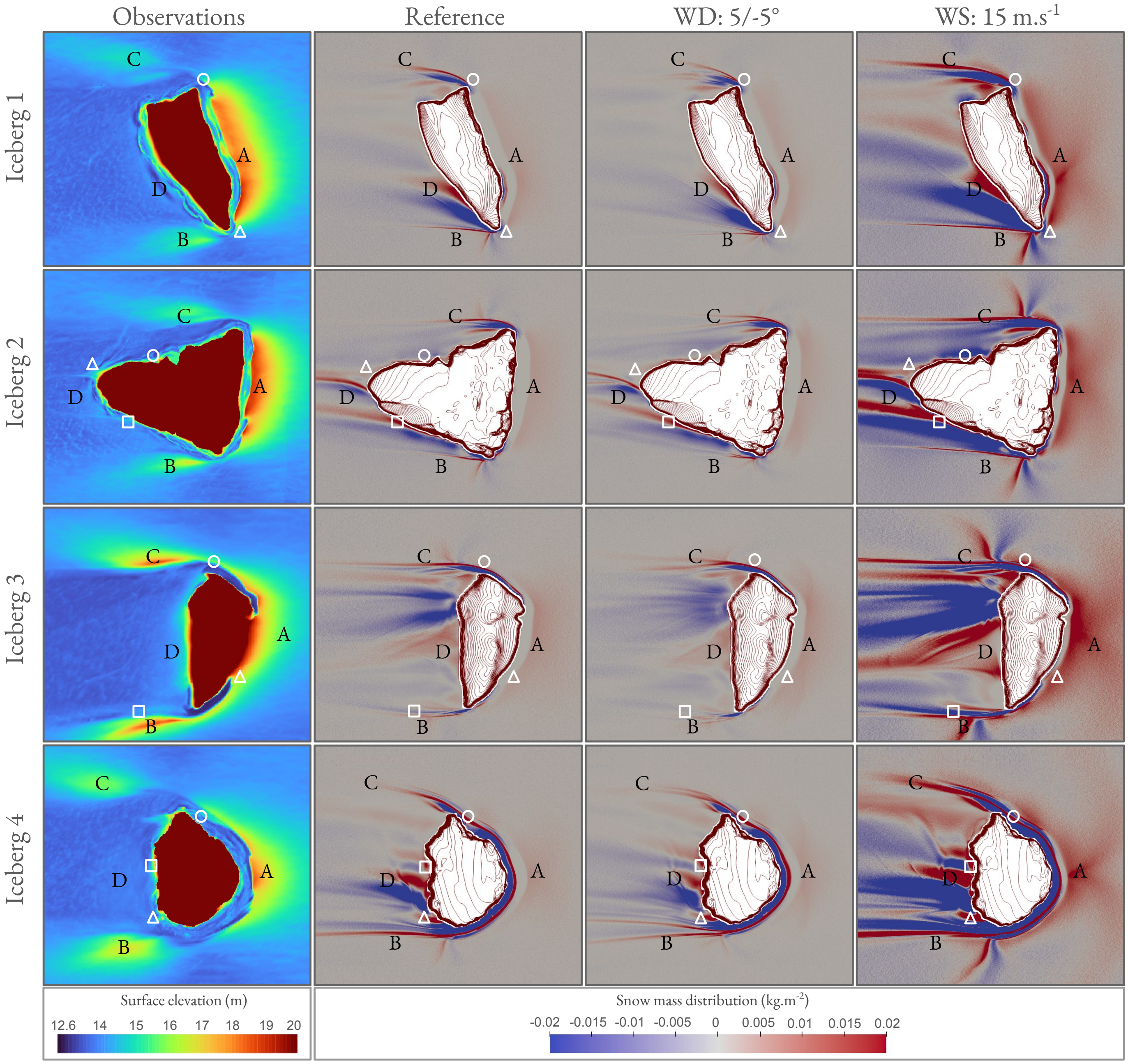

Fig. 3. Comparison between observations (first column) and model results for icebergs 1-4. The wind flows from right to left. The second column corresponds to the reference simulations highlighted in bold in Table 1 (wind direction: 0°, wind speed: 10 m.s^{-1}). The third column shows the combined model results for wind directions of -5° and 5°. The last column shows the results obtained with a higher wind speed (15 m.s^{-1}). Color bar limits are intentionally constrained for visualization purposes; localized values may exceed the displayed maximum.

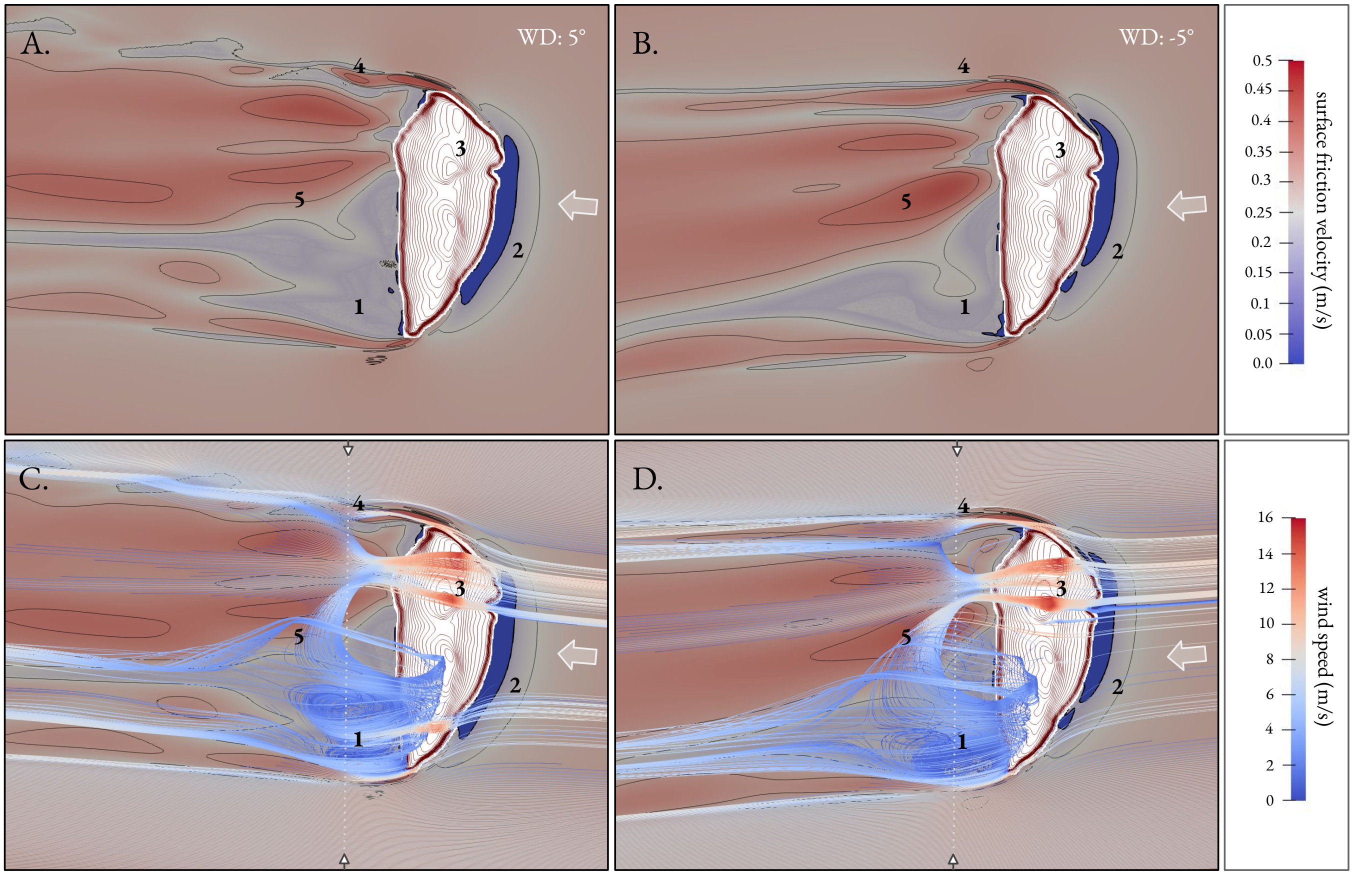

Fig. 4. Surface friction velocity fields and flow streamlines around Iceberg 3 simulated for wind directions of +5° (left column) and −5° (right column). The wind direction is indicated by the white arrows. The top panels (**A**, **B**) show surface friction velocity values in m.s^{-1}, where higher values (in red) typically correspond to zones of snow erosion. The bottom panels (**C**, **D**) display flow streamlines extracted along the dotted line at a height of 0.8 m, selected to capture representative flow behaviour in the lee of the iceberg. The color scheme corresponds to wind speed expressed in m.s^{-1}. Turbulent structures (eddies) are clearly visible in the wake of the iceberg for both wind directions.

4.2 Iceberg size effects

Observations show that iceberg size plays a key role in controlling the extent of snowdrift formation. Figure 5 displays a log-log plot of iceberg area versus snowdrift area, incorporating both model simulations (dotted line) and field measurements (solid line). The area is used for comparison to avoid converting between measured snow height and modelled snow mass (kg.m^{-2}), which would require snow density assumptions. The slope and intercepts of the regression lines are displayed in Table 2. Here, the focus is placed on comparing the slopes of the regression lines rather than their intercepts. The measured snowdrifts formed over longer time periods and under a broader range of cumulative wind conditions than those represented in the model simulations, which are limited to a single, short-duration wind forcing (300 s). As a result, the drift areas observed in the field are more spatially extensive, making the y-intercepts of the regressions non-comparable. In contrast, the regression slopes —capturing how snowdrift area scales with iceberg area— provide a valid basis for comparison between model and measurements.

In Table 2, the observational data exhibit a slope below one (0.81), indicating a sublinear relationship between the two variables. In other words, as iceberg area increases, the resulting snowdrift area expands at a proportionally reduced rate. When separating snowdrift accumulation data into windward and lateral/leeward components, both exhibit similar trends; however, the windward drift displays a slope closer to one ($0.94 > 0.70$), indicating a relationship that is nearer to linear. The fitted regression lines yield high coefficients of determination (R^2) across all measurement plots, offering strong evidence for a consistent scaling relationship between iceberg and snowdrift areas.

We seek to replicate the observed scaling relationship with our snow model and evaluate its ability to quantitatively simulate snowdrift. To this end, the four icebergs described earlier were scaled to different sizes, both smaller and larger than the original (details in Table A2). The use of consistent iceberg geometries across scales allows for a focused analysis of size effects, eliminating shape as a variable. Figure 6 shows the snow deposition areas for each iceberg size class, with Iceberg 3 as a representative example. Examining the windward accumulation (on the right of each subplot), it is evident that the accumulation area changes with iceberg size. For the largest iceberg (subplot D), the extent of windward accumulation is noticeably smaller. However, this trend is less clear for the other iceberg sizes, as the smallest iceberg (subplot A) shows reduced windward accumulation zones compared to the directly larger iceberg sizes (subplots B and C). One possible explanation is that snow particles in the smallest size class settle earlier in the flow, before reaching the iceberg. This results in a light, uniform deposition across the domain,

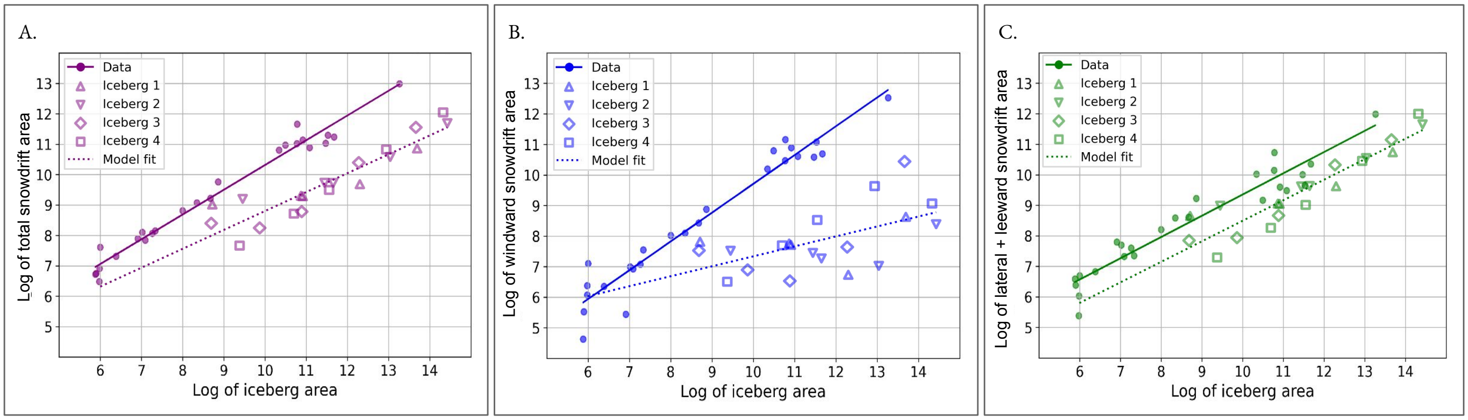

Fig. 5. Scaling relationships between iceberg area and snowdrift area, shown on a logarithmic scale. Observational data are represented by solid lines and filled circles, while model results are shown as dotted lines with unfilled markers. Each symbol corresponds to a specific iceberg, with increasing numerical size indicated by the sequence of data points. The three panels display relationships between iceberg area and (A) total snowdrift area, (B) windward snowdrift area, and (C) lateral and leeward snowdrift area, respectively. The corresponding regression slopes and intercepts are provided in Table 2 for the simulations and measurements.

limiting the amount of snow that can accumulate close to the windward side. These observations are illustrated in Figure 5.B, showing the iceberg area vs windward snowdrift area. The numerical data points exhibit considerable scatter, resulting in a lower slope and R^2 value compared to measurements. This means that the model-based relationship between iceberg and snowdrift areas is weaker and less defined than that in the observations. Although a few data points match the slope observed in the measurements, the model generally fails to replicate the scaling relationship for windward accumulation, due to the high variability in the model results.

When examining lateral and leeward snow accumulation, the model demonstrates improved performance. Figure 6 shows that as iceberg size increases, the lateral and leeward snow accumulation decreases relative to the iceberg size. For the largest iceberg (subplot D), lateral and leeward drifts are significantly smaller compared to those for the smaller icebergs, indicating a sublinear numerical relationship between iceberg size and snowdrift area. Figure 5.C supports the sublinear relationship for lateral and leeward snow accumulation, with the numerical slope of approximately 0.7 closely agreeing with the observed slope. The high coefficient of determination (R^2) further reinforces the idea that iceberg size plays a significant role in leeward snowdrift size, also within our numerical framework.

Table 2. Regression parameters (slope, intercept) and coefficient of determination (R^2) from the linear regressions applied to both modeling and observational data, detailed in Figure 5.

	Data Input	**Slope**	**Intercept**	**R-squared (R^2)**
Total	Observations	0.814	2.174	0.974
	Model	0.620	2.59	0.847
Windward	Observations	0.942	0.289	0.942
	Model	0.326	4.07	0.323
Lateral/ Leeward	Observations	0.696	2.395	0.917
	Model	0.671	1.78	0.862

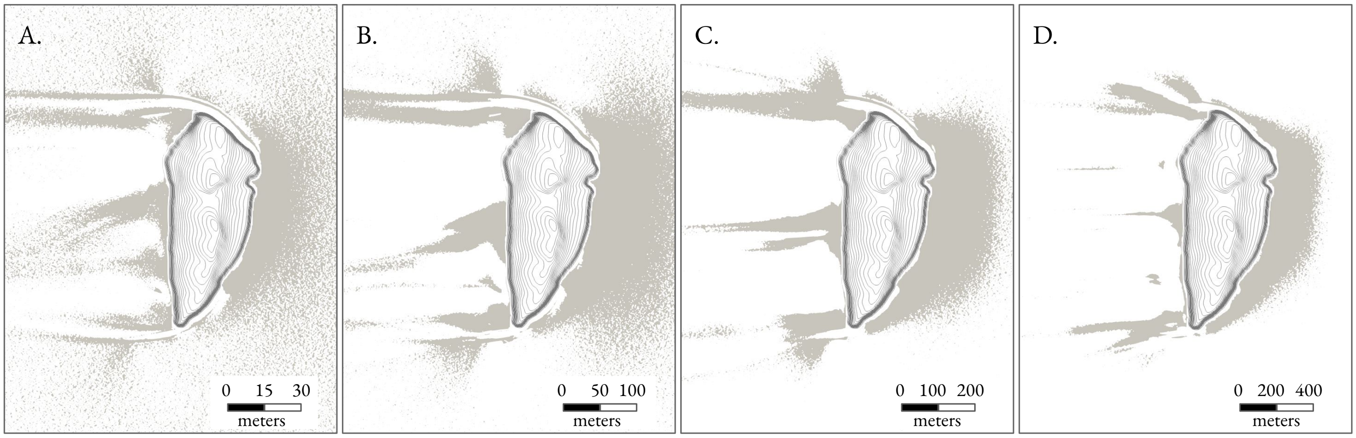

Fig. 6. Effect of iceberg size on snow drift size, shown for Iceberg 3, with increasing iceberg dimensions to the right. Snow deposition zones are shown in grey. The maximum horizontal extent (width) of the iceberg serves as reference, taking the following values: **A.** 125 m, **B.** 375 m, **C.** 750 m, **D.** 1500 m. Results are oriented similarly to the observations, with wind coming from the right.

5 DISCUSSION

This study applies the fluid dynamics-based, Eulerian–Lagrangian snow transport model snowBedFoam to investigate drifting snow patterns around Antarctic icebergs. The objectives are threefold: (1) to assess the agreement between modeled and observed snow distribution around icebergs, (2) to examine the influence of wind conditions on snowdrift formation, and (3) to explore the scaling relationship between iceberg size and snowdrift extent as well as its implications.

The strong agreement between modeled and observed drift patterns supports the conclusion that wind is the dominant factor shaping snow distribution around icebergs. The observed patterns typically display a characteristic structure: a broad deposition zone on the windward side, interrupted by a narrow wind scoop near the iceberg base; lateral drifts forming adjacent to and extending leeward of the icebergs; and a small accumulation zone immediately in the lee, followed by an elongated virtually snow free region downwind. The longitudinal and lateral development of these features is driven by variations in iceberg shape and prevailing atmospheric and surface conditions. Overall, the fluid dynamics model captures the general snow distribution patterns and can reproduce some of the fine-scale features with notable accuracy (e.g., Iceberg 2). However, discrepancies between modeled and observed results remain.

Simulations with a strictly perpendicular wind direction led to an overestimation of snow deposition in the direct lee of the icebergs compared to observations. However, when two varying, slightly non-normal wind directions were combined, their cumulative effects reduced deposition in this region, improving the match with the measurements. This suggests that natural fluctuations in wind directions would intensify erosion in the direct lee of icebergs, making the accumulated snow prone to removal during wind shifts. Besides, model simulations at varying nominal wind speeds showed that higher velocities increased snow accumulation near the iceberg base, reducing the extent of the adjacent wind scoop. This indicates that wind gusts frequently observed in Antarctica may drive the formation of snow bridges between iceberg edges and the surrounding snow cover (e.g., Iceberg 3). Moreover, the lateral and longitudinal spread of the snowdrifts, along with total accumulation, increased with wind speed. This aligns with prior research identifying wind speed as a governing factor in the magnitude of snowdrifts (Hames and others, 2025). The extent of snowdrift formation is thus primarily controlled by the maximum wind speed at a given location, making snowdrifts a persistent and direct indicator of local atmospheric conditions.

Given their sensitivity to wind parameters, snowdrifts offer valuable insights into regional weather patterns.

Regular remote sensing measurements of iceberg-affected areas could help monitor wind patterns in remote Antarctic regions with scarce on-site observations (Franke and others, 2025). Using time series of satellite imagery, changes in snow distribution can be identified over time. This approach could potentially improve our understanding of coastal weather patterns and provide crucial validation data for meso- and large-scale weather models, which often lack observations in these regions.

In addition to wind conditions, the relationship between iceberg size and associated snowdrift extent was investigated through numerical simulations. Log-log plots of measured iceberg area versus snowdrift area revealed a strong sublinear relationship, indicating that larger icebergs accumulate proportionally less snow relative to their size. This sublinear behavior was consistent across both windward and lateral/leeward drift regions. On the numerical side, the model reliably reproduced the empirical scaling of lateral and leeward snowdrifts across the simulated iceberg size range, but failed to do so for windward components. Simulated windward drift areas displayed considerable variability, with no evident scaling relationship to iceberg size in the scatter plots. The cause of this discrepancy is unclear, but it may stem from an inadequate representation of atmospheric turbulence and stability. In Antarctica, the typically stable and stratified boundary layer is expected to limit vertical mixing, resulting in higher near-surface particle concentrations and potentially increased accumulation on the windward side compared to neutral flow simulations. Moreover, preferential deposition from precipitation (Lehning and others, 2008) was excluded from the model due to computational constraints, although prior studies have demonstrated its significant contribution to windward snow accumulation (Hames and others, 2025). Further research and model adjustments are required to improve windward accumulation predictions. For lateral and leeward accumulation, model outputs closely matched observations, both exhibiting a power-law exponent of approximately 0.7. Thus, the scaling of leeward accumulation is more accurately captured by the current modeling approach.

The observed scaling relationship suggests a link between ice shelf calving dynamics and snow distribution over down-drift landfast sea ice. In particular, the degree of iceberg fragmentation —into fewer large or numerous smaller blocks— modulates snow accumulation for a given ice volume, shaping its overall impact on the surrounding sea ice. Recent studies have examined the impact of iceberg-induced snowdrifts on landfast ice, using microwave radar data from the ANTSI campaign over Atka Bay (Franke and others, 2025). Results show that sea ice properties are significantly impacted by the presence of icebergs and the snowdrifts they generate. This confirms the connection between continental ice shelf dynamics and Antarctic sea ice processes. On a broader scale, regional variations in iceberg size and concentration across

Antarctica may serve as proxies for sea ice properties and thickness, which affect seasonal ice dynamics and marine operations. Regions with few or no icebergs tend to have more uniform coastal snow and sea ice conditions, while areas with many small icebergs exhibit greater variability and heterogeneity. This effect is especially pronounced in regions with undeformed, level sea ice, where the lack of pressure ridges reduces other sources of heterogeneity in snow distribution (Langhorne and others, 2023). Further investigation is required to better understand the relationship between iceberg attributes and landfast sea ice properties. Such insights could improve our understanding of small-scale sea ice thickness distribution near land, supporting more effective marine navigation and operational planning.

Overall, this study advances our understanding of how iceberg characteristics and wind conditions modulate drifting snow dynamics in coastal Antarctic regions. Continued model development is needed to better capture windward accumulation and to more accurately quantify snow depth distribution near icebergs. Moreover, future work should focus on expanding the observational dataset to include iceberg-induced snowdrifts from other regions and to simulate a wider range of wind conditions. This would support a more robust quantification of the relationship between wind conditions and snowdrift extent, strengthening the potential of snowdrifts as measures of local atmospheric patterns.

6 CONCLUSION

Drifting snow and its associated mass redistribution play a critical role in shaping snow cover in Antarctic coastal regions, where landfast ice is a defining feature. In this sensitive environment, icebergs influence surface wind and sea ice flooding, which in turn affect snow stratification and ecological processes. However, their overall impact remains largely unknown. To address this, our study examined how variations in iceberg size and wind conditions shape snow distribution, using integrated observational data and numerical modeling. The alignment between modeled and observed snow distribution patterns suggests that drifting snow is the primary factor driving snow depth variability around icebergs. In particular, model runs show that changes in wind direction likely limit snow accumulation in the immediate lee of icebergs, where both observations and model results reveal pronounced erosion. Simulations further highlight wind speed as a critical factor controlling the maximum extent of snowdrifts, both laterally and along the flow direction. Consequently, peak wind speed is essential for estimating the total surface area of snow cover affected by icebergs. In parallel, results indicate that larger icebergs accumulate less snow per unit size than smaller icebergs, pointing to a sublinear relationship between iceberg and snowdrift sizes. These findings have broader implications, as the snow depth variability driven by icebergs impacts the sea ice beneath. Icebergs formed by ice shelf calving thus serve as a bridge between ice shelf and sea ice processes, with their size determining the total snow accumulation. Moreover, the sensitivity of snowdrifts to wind parameters makes them an ideal proxy of regional weather patterns. Circumpolar remote sensing observations of these snowdrifts could provide valuable validation for Antarctic weather models along the coastline. Despite its limitations, this work serves as an important first step in understanding snow distribution around icebergs and their role in the snow and sea ice mass balance of Antarctic coastal regions.

7 ACKNOWLEDGEMENTS

We thank the AWI polar aircraft technicians Cristina Sans Coll and Clemens Gollin for their support in the field during the 2022/23 UWBM radar flights as well as the Kenn Borek flight crew Alan Gilbertson (Captain), Noah Hladiuk (First Officer) and Brad Friesen (AME). Logistical support in the field for the airborne radar campaign has been provided by Neumayer III Station (Germany) and Troll Station (Norway). Furthermore, we are grateful for the logistics support and infrastructure for the ground-based survey on Atka Bay provided by AWI and the welcoming staff at Neumayer III Station.

For the ANTSI 2022/23 airborne campaign, we acknowledge support via the AWI_PA_02135 funding grant from AWI. Océane Hames was funded by the AWI ANT-LAND funding grant AWI_ANT_27. Together with Iolène Bouzdine, part of her funding also comes from the SNSF funding grants SNF 200020_215406. This work was supported by a grant from the Swiss National Supercomputing Centre (CSCS) under project ID s1308 on Alps. Finally, the authors thank Mahdi Jafari for his input on the modeling work, as well as Steven Franke for constructive discussions on snowdrifts over landfast sea ice.

REFERENCES

Achter GV, Fichefet T, Goosse H, Pelletier C, Sterlin J, Huot P, Lemieux J, Fraser A, Haubner K and Porter-Smith R (2022) Modelling landfast sea ice and its influence on ocean–ice interactions in the area of the totten glacier, east antarctica. *Ocean Modelling*, **169**, 101920 (doi: 10.1016/j.ocemod.2021.101920)

Anderson RS and Haff PK (1991) Wind modification and bed response during saltation of sand in air. In OE Barndorff-Nielsen and BB Willetts (eds.), *Aeolian Grain Transport 1*, 21–51, Springer, Vienna, ISBN 978-3-7091-6706-9 (doi: 10.1007/978-3-7091-6706-9_2)

Arndt S, Hoppmann M, Schmithüsen H, Fraser AD and Nicolaus M (2020) Seasonal and interannual variability of landfast sea ice in Atka Bay, Weddell Sea, Antarctica. *The Cryosphere*, **14**(9), 2775–2793 (doi: 10.5194/tc-14-2775-2020)

Bagnold RA (1941) The Physics of Blown Sand and Desert Dunes

Beyers JHM (2004) Numerical modelling of the snow flow characteristics surrounding Sanae IV Research Station, Antarctica. Available at: http://hdl.handle.net/10019.1/15935

Comola F and Lehning M (2017) Energy- and momentum-conserving model of splash entrainment in sand and snow saltation. *Geophysical Research Letters*, **44**(3), 1601–1609, ISSN 1944-8007 (doi: 10.1002/2016GL071822)

Doorschot JJJ and Lehning M (2002) Equilibrium Saltation: Mass Fluxes, Aerodynamic Entrainment, and Dependence on Grain Properties. *Boundary-Layer Meteorology*, **104**(1), 111–130, ISSN 1573-1472 (doi: 10.1023/A:1015516420286)

Fernandes C, Semyonov D, Ferrás LL and Nóbrega JM (2018) Validation of the CFD-DPM solver DPMFoam in OpenFOAM through analytical, numerical and experimental comparisons. *Granular Matter*, **20**(4), 64, ISSN 1434-7636 (doi: 10.1007/s10035-018-0834-x)

Franke J and Baklanov A (2007) Best Practice Guideline for the CFD Simulation of Flows in the Urban Environment: COST Action 732 Quality Assurance and Improvement of Microscale Meteorological Models

Franke S, Neudert M, Helm V, Jutila A, Hames O, Neckel N, Arndt S and Haas C (2025) Iceberg influence on snow distribution and slush formation on Antarctic landfast sea ice from airborne multi-sensor observations. *EGUsphere*, **2025**, 1–30 (doi: 10.5194/egusphere-2025-2657)

Fraser A, Massom R, Handcock MS, Reid P, Ohshima KI, Raphael M, Cartwright J, Klekociuk A, Wang Z and Porter-Smith R (2021) Eighteen-year record of circum-antarctic landfast-sea-ice distribution allows detailed baseline characterisation and reveals trends and variability. *The Cryosphere*, **15**, 5061–5077 (doi: 10.5194/tc-15-5061-2021)

Fraser AD, Wongpan P, Langhorne PJ, Klekociuk AR, Kusahara K, Lannuzel D, Massom RA, Meiners KM, Swadling KM, Atwater DP, Brett GM, Corkill M, Dalman LA, Fiddes S, Granata A, Guglielmo L, Heil P, Leonard GH, Mahoney AR, McMinn A, van der Merwe P, Weldrick CK and Wienecke B (2023) Antarctic Landfast Sea Ice: A Review of Its Physics, Biogeochemistry and Ecology. *Reviews of Geophysics*, **61**(2), e2022RG000770 (doi: https://doi.org/10.1029/2022RG000770), e2022RG000770 2022RG000770

González J, Almeida Ed and Gutiérrez A (2024) Wind farm power curve characterization under different atmospheric stability regimes. *Wind Engineering*, **48**, 1174–1185 (doi: 10.1177/0309524x241254473)

Groot Zwaaftink CD, Mott R and Lehning M (2013) Seasonal simulation of drifting snow sublimation in Alpine terrain. *Water Resources Research*, **49**(3), 1581–1590, ISSN 1944-7973 (doi: 10.1002/wrcr.20137), _eprint: https://onlinelibrary.wiley.com/doi/pdf/10.1002/wrcr.20137

Haas C (2023) ANTSI – ANTarctic Sea Ice and platelet ice survey (Polar 5 sea ice survey campaign 2022 Dronning Maud Land, Antarctica). `https://download.pangaea.de/reference/118209/attachments/WeeklyReport_3_ANTSI2022.pdf`, field report, Alfred Wegener Institute

Hames O, Jafari M and Lehning M (2021) snowBedFoam: an OpenFOAM Eulerian-Lagrangian solver for modelling snow transport (doi: http://dx.doi.org/10.16904/envidat.223)

Hames O, Jafari M, Wagner DN, Raphael I, Clemens-Sewall D, Polashenski C, Shupe MD, Schneebeli M and Lehning M (2022) Modeling the small-scale deposition of snow onto structured Arctic sea ice during a MOSAiC storm using snowBedFoam 1.0. *Geoscientific Model Development*, **15**(16), 6429–6449, ISSN 1991-959X (doi: 10.5194/gmd-15-6429-2022), publisher: Copernicus GmbH

Hames O, Jafari M, Köhler P, Haas C and Lehning M (2025) Governing Processes of Structure-Borne Snowdrifts: A Case Study at Neumayer Station III. *Journal of Geophysical Research: Earth Surface*, **130**(3), e2024JF008180 (doi: https://doi.org/10.1029/2024JF008180), e2024JF008180 2024JF008180

Hargreaves DM and Wright NG (2007) On the use of the k-ϵ model in commercial CFD software to model the neutral atmospheric boundary layer. *Journal of Wind Engineering and Industrial Aerodynamics*, **95**(5), 355–369, ISSN 0167-6105 (doi: 10.1016/j.jweia.2006.08.002)

Hutter N, Hendricks S, Jutila A, Ricker R, von Albedyll L, Birnbaum G and Haas C (2023) Digital elevation models of the sea-ice surface from airborne laser scanning during MOSAiC. *Scientific Data*, **10**(1), 729, ISSN 2052-4463 (doi: 10.1038/s41597-023-02565-6)

Klöwer M, Jung T, König-Langlo G and Semmler T (2013) Aspects of weather parameters at Neumayer station, Antarctica, and their representation in reanalysis and climate model data. *Meteorologische Zeitschrift*, **22**(6), 699–709 (doi: 10.1127/0941-2948/2013/0505)

Langhorne PJ, Haas C, Price D, Rack W, Leonard GH, Brett GM and Urbini S (2023) Fast Ice Thickness Distribution in the Western Ross Sea in Late Spring. *Journal of Geophysical Research: Oceans*, **128**(2), e2022JC019459 (doi: https://doi.org/10.1029/2022JC019459), e2022JC019459 2022JC019459

Launder BE and Spalding DB (1974) The numerical computation of turbulent flows. *Computer Methods in Applied Mechanics and Engineering*, **3**(2), 269–289, ISSN 0045-7825 (doi: 10.1016/0045-7825(74)90029-2)

Lehning M, Löwe H, Ryser M and Raderschall N (2008) Inhomogeneous precipitation distribution and snow transport in steep terrain. *Water Resources Research*, **44**(7), ISSN 1944-7973 (doi: 10.1029/2007WR006545)

Lei R, Li Z, Cheng B, Zhang Z and Heil P (2010) Annual cycle of landfast sea ice in Prydz Bay, east Antarctica. *Journal of Geophysical Research: Oceans*, **115**(C2) (doi: https://doi.org/10.1029/2008JC005223)

Massom R, Giles AB, Fricker HA, Warner R, Legrésy B, Hyland G, Young NW and Fraser A (2010) Examining the interaction between multi-year landfast sea ice and the Mertz Glacier tongue, East Antarctica: another factor in ice sheet stability? *Journal of Geophysical Research: Oceans*, **115** (doi: 10.1029/2009jc006083)

Melo DB, Sharma V, Comola F, Sigmund A and Lehning M (2022) Modeling Snow Saltation: The Effect of Grain Size and Interparticle Cohesion. *Journal of Geophysical Research: Atmospheres*, **127**(1), e2021JD035260, ISSN 2169-8996 (doi: 10.1029/2021JD035260), _eprint: https://onlinelibrary.wiley.com/doi/pdf/10.1029/2021JD035260

Moukalled F, Mangani L and Darwish M (2015) The Finite Volume Method in Computational Fluid Dynamics: An Advanced Introduction with OpenFOAM® and Matlab® (doi: 10.1007/978-3-319-16874-6)

Nihashi S and Ohshima K (2015) Circumpolar mapping of antarctic coastal polynyas and landfast sea ice: relationship and variability. *Journal of Climate*, **28**, 3650–3670 (doi: 10.1175/jcli-d-14-00369.1)

Orheim O, Giles A, Moholdt G, Jacka T and Bjørdal A (2022) Antarctic iceberg distribution revealed through three decades of systematic ship-based observations in the scar international iceberg database. *Journal of Glaciology*, **69**, 551–565 (doi: 10.1017/jog.2022.84)

Pomeroy JW and Gray DM (1990) Saltation of snow. *Water Resources Research*, **26**(7), 1583–1594 (doi: https://doi.org/10.1029/WR026i007p01583)

Pope SB (2000) *Turbulent Flows*. Cambridge University Press

Richards PJ and Hoxey RP (1993) Appropriate boundary conditions for computational wind engineering models using the k-ϵ turbulence model. *Journal of Wind Engineering and Industrial Aerodynamics*, **46-47**, 145–153, ISSN 0167-6105 (doi: 10.1016/0167-6105(93)90124-7)

Sharma V, Comola F and Lehning M (2018) On the suitability of the Thorpe–Mason model for calculating sublimation of saltating snow. *The Cryosphere*, **12**(11), 3499–3509, ISSN 1994-0416 (doi: 10.5194/tc-12-3499-2018), publisher: Copernicus GmbH

The OpenFOAM Foundation (2021) OpenFOAM: The Open Source CFD Toolbox. Available at: https://www.openfoam.com

The OpenFOAM Foundation (2025a) Foam::nutkAtmRoughWallFunctionFvPatchScalarField class documentation

The OpenFOAM Foundation (2025b) OpenFOAM Time Class Reference. Available at: *https : //cpp.openfoam.org/v12/classFoam_1_1Time.html#details*

Tomas J, Pourquié M and Jonker HJJ (2016) Stable stratification effects on flow and pollutant dispersion in boundary layers entering a generic urban environment. *Boundary-Layer Meteorology*, **159**, 221–239 (doi: 10.1007/s10546-015-0124-7)

Tominaga Y (2018) Computational fluid dynamics simulation of snowdrift around buildings: Past achievements and future perspectives. *Cold Regions Science and Technology*, **150**, 2–14, ISSN 0165-232X (doi: 10.1016/j.coldregions.2017.05.004)

Tominaga Y, Okaze T and Mochida A (2011) CFD modeling of snowdrift around a building: An overview of models and evaluation of a new approach. *Building and Environment*, **46**(4), 899–910, ISSN 0360-1323 (doi: https://doi.org/10.1016/j.buildenv.2010.10.020)

Wang Z and Huang N (2017) Numerical simulation of the falling snow deposition over complex terrain. *Journal of Geophysical Research: Atmospheres*, **122**(2), 980–1000 (doi: https://doi.org/10.1002/2016JD025316)

Wesche C, Weller R, König-Langlo G, Fromm T, Eckstaller A, Nixdorf U and Kohlberg E (2016) Neumayer III and Kohnen Station in Antarctica operated by the Alfred Wegener Institute. *Journal of large-scale research facilities JLSRF*, **2**, A85–A85, ISSN 2364-091) (doi: 10.17815/jlsrf-2-152)

Zhao J, Cheng B, Vihma T, Lü P, Han H and Shu Q (2022) The internal melting of landfast sea ice in prydz bay, east antarctica. *Environmental Research Letters*, **17**, 074012 (doi: 10.1088/1748-9326/ac76d9)

A APPENDIX

Table A1. Model parameters, coefficients, and boundary conditions used in the `snowBedFoam` simulations.

Parameter	**Symbol**	**Value**	**Unit**
Turbulence model settings			
Turbulence model	—	k-ϵ	—
Model coefficient	C_μ	0.09	—
Model coefficient	C_1	1.44	—
Model coefficient	C_2	1.92	—
Turbulent viscosity	ν_f	1.5×10^{-5}	m^2/s
Von Kármán constant	κ	0.4	—
Forcing conditions			
Air density	ρ_f	1.4	kg/m^3
Wind speed (10 m)	WS	10, 15	m/s
Wind direction (10 m)	WD	-5, 0, 5	°
Surface roughness length	z_0	10^{-3}	m
Vertical coordinate	z	10	m
Particle properties			
Particle density	ρ_p	918	kg/m^3
Mean diameter	d_m	150	μm
Min diameter	d_{min}	50	μm
Max diameter	d_{max}	500	μm
Diameter std. deviation	σ_d	50	μm
Bed cohesion	ϕ	10^{-10}	J
Rebound KE fraction	ϵ_r	0.25	—
Rebound momentum fraction	μ_r	$\sqrt{\epsilon_r}$	—
Friction KE fraction	ϵ_f	$0.96(1 - P_r \epsilon_r)$	—
Friction momentum fraction	μ_f	0.4	—
Simulation time			
Flow initialization	—	100	s
Two-phase simulation time	—	200	s
Total simulation time	—	300	s

Table A2. Model runs performed for Iceberg 1-4, with the reference simulations highlighted in bold. The dimensions have been rounded for simplicity.

Run name	Iceberg	Size class	Dimensions (m)			Wind speed (m.s^{-1})	Wind direction (°)
			X	Y	H		
icb1__size1__ws10__wd0	**1**	**ref**	**214**	**367**	**35**	**10**	**0**
icb1__size1__ws15__wd0	1	ref	·	·	·	15	0
icb1__size1__ws10__wd5	1	ref	·	·	·	10	5, −5
icb1__size2__ws10__wd0	1	2	73	125	12	10	0
icb1__size3__ws10__wd0	1	3	219	375	36	10	0
icb1__size4__ws10__wd0	1	4	437	750	72	10	0
icb1__size5__ws10__wd0	1	5	877	1500	144	10	0
icb2__size1__ws10__wd0	**2**	**ref**	**381**	**338**	**28**	**10**	**0**
icb2__size1__ws15__wd0	2	ref	·	·	·	15	0
icb2__size1__ws10__wd5	2	ref	·	·	·	10	5, −5
icb2__size2__ws10__wd0	2	2	141	125	10	10	0
icb2__size3__ws10__wd0	2	3	423	375	31	10	0
icb2__size4__ws10__wd0	2	4	845	750	63	10	0
icb2__size5__ws10__wd0	2	5	1691	1500	125	10	0
icb3__size1__ws10__wd0	**2**	**ref**	**102**	**225**	**24**	**10**	**0**
icb3__size1__ws15__wd0	3	ref	·	·	·	15	0
icb3__size1__ws10__wd5	3	ref	·	·	·	10	5, −5
icb3__size2__ws10__wd0	3	2	57	125	13	10	0
icb3__size3__ws10__wd0	3	3	170	375	40	10	0
icb3__size4__ws10__wd0	3	4	340	750	80	10	0
icb3__size5__ws10__wd0	3	5	680	1500	160	10	0
icb4__size1__ws10__wd0	**2**	**ref**	**176**	**245**	**39**	**10**	**0**
icb4__size1__ws15__wd0	4	ref	·	·	·	15	0
icb4__size1__ws10__wd5	4	ref	·	·	·	10	5, −5
icb4__size2__ws10__wd0	4	2	91	125	20	10	0
icb4__size3__ws10__wd0	4	3	269	375	60	10	0
icb4__size4__ws10__wd0	4	4	539	750	119	10	0
icb4__size5__ws10__wd0	4	5	1077	1500	238	10	0